

RESEARCH ARTICLE



## Design, synthesis and evaluation of $^{18}\text{F}$ -labeled cationic carbonic anhydrase IX inhibitors for PET imaging

Zhengxing Zhang<sup>a\*</sup>, Joseph Lau<sup>a\*</sup>, Chengcheng Zhang<sup>a</sup>, Nadine Colpo<sup>a</sup>, Alessio Nocentini<sup>b</sup>, Claudiu T. Supuran<sup>b</sup>, François Bénard<sup>a,c,d</sup> and Kuo-Shyan Lin<sup>a,c,d</sup>

<sup>a</sup>Department of Molecular Oncology, BC Cancer Agency, Vancouver, British Columbia, Canada; <sup>b</sup>Department of Neurofarba, Section of Pharmaceutical and Nutriceutical Sciences, Università Degli Studi Di Firenze, Florence, Italy; <sup>c</sup>Department of Functional Imaging, BC Cancer Agency, Vancouver, British Columbia, Canada; <sup>d</sup>Department of Radiology, University of British Columbia, Vancouver, British Columbia, Canada

### ABSTRACT

Carbonic anhydrase IX (CA-IX) is a marker for tumor hypoxia, and its expression is negatively correlated with patient survival. CA-IX represents a potential target for eliminating hypoxic cancers. We synthesized fluorinated cationic sulfonamide inhibitors **1–3** designed to target CA-IX. The binding affinity for CA-IX ranged from 0.22 to 0.96  $\mu\text{M}$ . We evaluated compound **2** as a diagnostic PET imaging agent. Compound **2** was radiolabeled with  $^{18}\text{F}$  in  $10 \pm 4\%$  decay-corrected radiochemical yield with  $85.1 \pm 70.3$  GBq/ $\mu\text{mol}$  specific activity and  $>98\%$  radiochemical purity.  $^{18}\text{F}$ -labeled **2** was stable in mouse plasma at  $37^\circ\text{C}$  after 1 h incubation. PET/CT imaging was conducted at 1 h post-injection in a human colorectal cancer xenograft model.  $^{18}\text{F}$ -labeled **2** cleared through hepatobiliary and renal pathways. Tumor uptake was approximately  $0.41 \pm 0.06\%$  ID/g, with a tumor-to-muscle ratio of  $1.99 \pm 0.25$ . Subsequently, tumor xenografts were visualized with moderate contrast. This study demonstrates the use of a cationic motif for conferring isoform selectivity for CA-IX imaging agents.

### ARTICLE HISTORY

Received 10 March 2017  
Revised 15 March 2017  
Accepted 16 March 2017

### KEYWORDS

Carbonic anhydrase IX; fluorine-18; molecular imaging; positron emission tomography

### Introduction



Tumor cells cycle through stages of being well-oxygenated or oxygen-deprived. Hypoxia occurs when oxygen level of the micro-environment is unable to sustain the metabolic demands of a growing tumor<sup>1</sup>. Regardless of size, stage, grade, or histology, all solid tumors are susceptible to hypoxia<sup>2</sup>. Although hypoxia may initially limit growth potential, it also promotes and regulates biological processes like angiogenesis, invasiveness, metastasis, metabolism, and genomic instability<sup>3</sup>. Moreover, hypoxia confers resistance and insensitivity to conventional chemotherapy and radiotherapy<sup>3,4</sup>. As such, therapeutic strategies targeting hypoxia and/or components of the hypoxia-induced signaling pathway are consistently being explored<sup>3</sup>. Inherently, there is a need to develop companion diagnostics that can be used for patient stratification or treatment response assessment.

An established surrogate marker for hypoxia is carbonic anhydrase IX (CA-IX). CA-IX is the protein that is most strongly upregulated by hypoxia and hypoxia-inducible factor  $1\alpha$  (HIF- $1\alpha$ )<sup>5</sup>. CA-IX is 1 of 15 unique but closely related zinc metalloenzymes<sup>6</sup>. Of the pertinent isoforms, CA-IX is preferentially expressed in solid malignancies to maintain intracellular pH homeostasis in concert with ion transporter systems<sup>7–11</sup>. In preclinical studies, attenuation of CA-IX activity by small molecule inhibitors has been shown to be efficacious in reducing primary tumor growth and distant metastases<sup>12–15</sup>. CA-IX inhibitors have also been used as delivery vectors of cytotoxic payloads to target tumor cells within hypoxic niches<sup>16–18</sup>. Complementing these therapeutic efforts has been the development of CA-IX radiotracers derived from inhibitors for

positron emission tomography (PET) and single photon emission computed tomography (SPECT) applications<sup>19–31</sup>. PET and SPECT can generate images of high resolution and sensitivity, while providing quantitative information on drug target expression.

CA-IX is an attractive target because of its pathological expression in cancers, as well as the fact that it resides as a cell surface transmembrane protein<sup>6</sup>. However, the highly conserved catalytic domain shared by CA isoforms poses as a challenge for synthesizing CA-IX selective imaging agents<sup>6</sup>. Off-target binding to intracellular CAs, notably CA-I and CA-II expressed in erythrocytes, can reduce tumor targeting and contrast ratios<sup>6</sup>. Therefore, strategies to confer CA-IX selectivity for small molecule inhibitors have focused on limiting transport across the plasma membrane. Previously, our research group reported two approaches for sulfonamide-based CA-IX imaging agents that successfully targeted human colorectal cancer xenografts. In one approach, we leveraged a multimeric design to synthesize  $^{18}\text{F}$ -labeled trivalent tracers (Figure 1(A)) that were of sufficient bulk (MW  $>1$  kDa) to be cell-impermeable<sup>26</sup>. In the other approach, we conjugated pharmacophores to different polyaminocarboxylate chelators for  $^{68}\text{Ga}$ -radiolabeling (Figure 1(B))<sup>27</sup>. The hydrophilicity of the metal/chelator complex facilitated selective targeting of CA-IX *in vivo*.

In addition to factors like size and hydrophilicity, the overall charge of a molecule can modulate the property to permeate through the plasma membrane. Previous work published by Casey et al.<sup>32</sup> demonstrated that cationic sulfonamide derivatives showed favorable CA-IX inhibition profiles (Figure 1(C)). As charged molecules, these inhibitors have limited transcellular uptake<sup>33</sup>. In this paper, we investigated if fluorinated sulfonamide

**CONTACT** Kuo-Shyan Lin  [klin@bccrc.ca](mailto:klin@bccrc.ca)  675 West 10th Avenue, Rm 4-123, Vancouver, BC V5Z 1L3, Canada

\*These two authors contributed equally to this work.

© 2017 The Author(s). Published by Informa UK Limited, trading as Taylor & Francis Group.

This is an Open Access article distributed under the terms of the Creative Commons Attribution License (<http://creativecommons.org/licenses/by/4.0/>), which permits unrestricted use, distribution, and reproduction in any medium, provided the original work is properly cited.

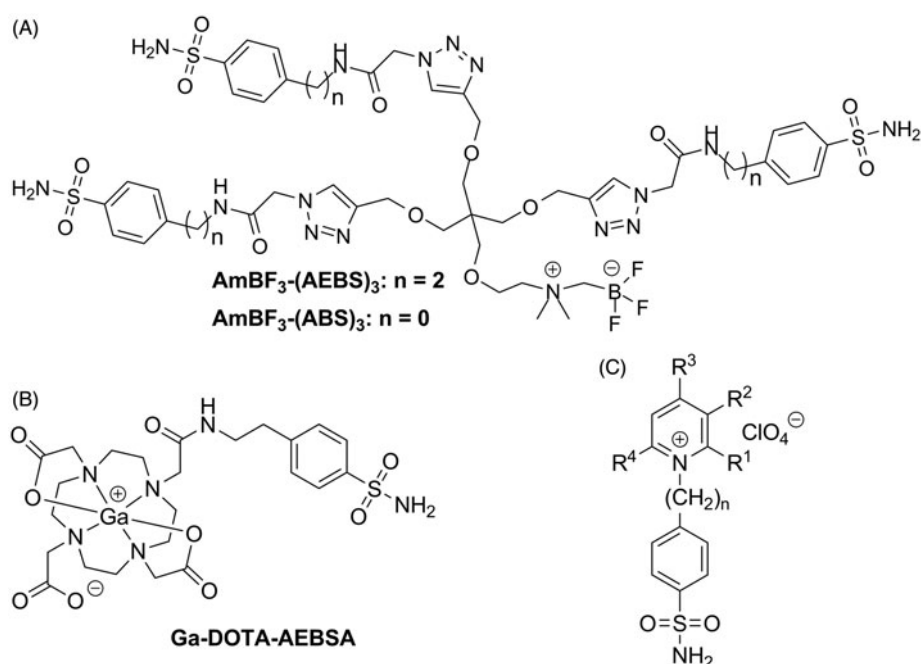


**Figure 1.** Reported sulfonamide derivatives that are CA-IX selective agents. (A) Trimeric  $\text{AmBF}_3\text{-(AEBS)}_3$  and  $\text{AmBF}_3\text{-(ABS)}_3$ , (B) Ga-DOTA-AEBSA, and (C) cationic sulfonamide derivatives.

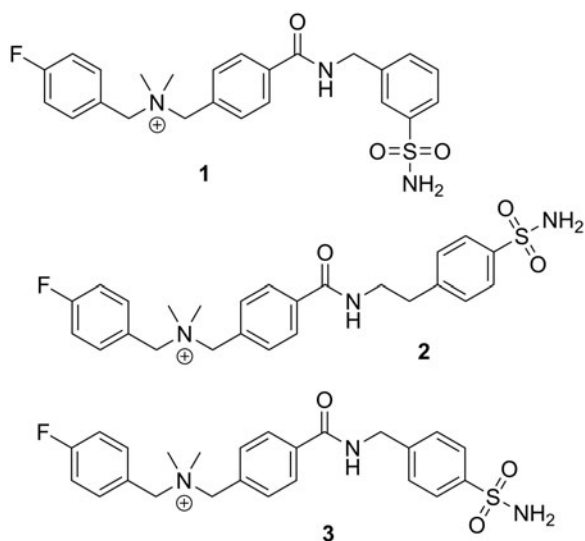


**Figure 2.** Chemical structures of three cationic carbonic anhydrase IX inhibitors evaluated in this study.

derivatives engrafted with a cationic motif can be used as potential PET tracers for imaging CA-IX expression in tumors (Figure 2).

## Materials and methods

### Chemicals and instrumentation

All chemicals and solvents were obtained from commercial sources, and used without further purification. Triethylammonium phosphate buffer (TEA-PB, pH 7.29) was prepared by titrating a solution of triethylamine (8 mL) in deionized water (1 L) with *o*-phosphoric acid monitored using a Denver Instrument (Bohemia, NY) UltraBasic Benchtop pH meter. Proton NMR spectra were obtained using a Bruker (Billerica, MA) Avance 400inv Spectrometer, and are reported in parts per million. Mass analyses were performed using an AB SCIEX (Framingham, MA) 4000 QTRAP mass spectrometer system

with an ESI ion source. Melting points were taken on a Fisher–Johns melting point apparatus (Fisher Scientific, Pittsburgh, PA) and were uncorrected. The quaternary methyl ammonium (QMA) anion exchange and C18 light Sep-Pak cartridges (1 cm<sup>3</sup>, 50 mg) were obtained from Waters (Milford, MA). Purification and quality control of <sup>18</sup>F-labeled **2** were performed on an Agilent (Santa Clara, CA) HPLC system equipped with a model 1200 quaternary pump, a model 1200 UV absorbance detector, and a Bioscan (Washington, DC) NaI scintillation detector. The radio-detector was connected to a Bioscan B-FC-1000 Flow-count system, and the output from the Bioscan Flow-count system was fed into an Agilent 35900E Interface, which converted the analog signal to digital signal. The operation of the Agilent HPLC system was controlled using the Agilent ChemStation software. The HPLC columns used were a semi-preparative column (Phenomenex C18, 5 μ, 250 × 10 mm) and an analytical column (Phenomenex C18, 5 μ, 250 × 4.6 mm). <sup>18</sup>F-Fluoride was produced by the <sup>18</sup>O(p, n)<sup>18</sup>F reaction using an Advanced Cyclotron Systems Inc. (Richmond, BC, Canada) TR19 cyclotron. Radioactivity of <sup>18</sup>F-labeled **2** was measured using a Capintec (Ramsey, NJ) CRC<sup>®</sup>-25 R/W dose calibrator, and the radioactivity of mouse tissues collected from biodistribution studies were counted using a Perkin Elmer (Waltham, MA) Wizard2 2480 automatic gamma counter. PET imaging experiments were conducted using a Siemens (Knoxville, TN) Inveon microPET/CT scanner.

### Syntheses of precursors and standards

#### 2,3,5,6-Tetrafluorophenyl 4-[(dimethylamino) methyl] benzoate (**4**)

A mixture of 4-[(dimethylamino) methyl] benzoic acid hydrochloride (2.37 g, 11 mmol), 2,3,5,6-tetrafluorophenol (1.99 g, 12 mmol), and *N,N*-diisopropylethylamine (1.42 g, 11 mmol) in dichloromethane (80 mL) was added *N,N'*-dicyclohexylcarbodiimide (2.06 g, 10 mmol). After stirring at room temperature for 27 h, the reaction mixture was filtered, and the filtrate was extracted with 2 M NaOH aqueous solution (100 mL). The organic phase was dried with anhydrous magnesium sulfate, and evaporated under reduced

pressure. The residue was dissolved in 1:1 diethyl ether/hexane (100 mL), and the insoluble crystals were removed by filtration. The filtrate was concentrated under reduced pressure to yield **4** as colorless oil (3.25 g, 99%).  $^1\text{H NMR}$  (300 MHz,  $\text{CDCl}_3$ )  $\delta$  8.17 (d,  $J=8.3$  Hz, 2H), 7.50 (d,  $J=8.3$  Hz, 2H), 7.04 (tt,  $J=9.9$ , 7.0 Hz, 1H), 3.53 (s, 2H), 2.27 (s, 6H). MS (ESI) calculated for  $\text{C}_{16}\text{H}_{13}\text{F}_4\text{NO}_2$  327.1, found  $(\text{M} + \text{H})^+$  328.0.

***N,N*-dimethyl-*N*-(4-fluoro)benzyl-4-[(2,3,5,6-tetrafluorophenoxy) carbonyl] benzylammonium bromide (5)**

4-Fluorobenzyl bromide (236  $\mu\text{L}$ , 359 mg, 1.9 mmol) was added to a solution of **4** in acetonitrile (6 mL). The reaction mixture was stirred at room temperature for 3 days. The precipitated product was filtered, and washed with diethyl ether (2 mL  $\times$  3) to yield **5** as white powder (852 mg, 87%).  $^1\text{H NMR}$  (300 MHz, DMSO)  $\delta$  8.33 (d,  $J=8.3$  Hz, 2H), 8.05 (tt,  $J=10.9$ , 7.5 Hz, 1H), 7.89 (d,  $J=8.3$  Hz, 2H), 7.67 (dd,  $J=8.6$ , 5.5 Hz, 2H), 7.38 (t,  $J=8.8$  Hz, 2H), 4.74 (s, 2H), 4.65 (s, 2H), 2.93 (s, 6H). MS (ESI) calculated for  $\text{C}_{23}\text{H}_{19}\text{F}_5\text{NO}_2^+$  436.1, found  $(\text{M})^+$  435.8. Melting point: 198  $^\circ\text{C}$ .

***N*-4-[[[3-(aminosulfonyl) benzyl] amino] carbonyl] benzyl-*N,N*-dimethyl-4-fluorobenzylammonium bromide (1)**

A solution of **5** (155 mg, 0.3 mmol) and 3-(aminomethyl) benzenesulfonamide (80 mg, 0.43 mmol) in methanol (5 mL) was stirred at room temperature for 2 days. The solvent was removed by heating at 70  $^\circ\text{C}$ . Tetrahydrofuran (2 mL) was added to the residue, and the resulting mixture was heated at 70  $^\circ\text{C}$  for 2 min. The insoluble product was isolated by filtration to yield **1** as white solid (156 mg, 97%).  $^1\text{H NMR}$  (300 MHz, DMSO)  $\delta$  9.32 (t,  $J=5.9$  Hz, 1H), 8.04 (d,  $J=8.2$  Hz, 2H), 7.78 (s, 1H), 7.75–7.68 (m, 3H), 7.68–7.63 (m, 2H), 7.58–7.51 (m, 2H), 7.44–7.29 (m, 4H), 4.65 (s, 2H), 4.64 (s, 2H), 4.57 (d,  $J=5.8$  Hz, 2H), 2.89 (s, 6H). MS (ESI) calculated for  $\text{C}_{24}\text{H}_{27}\text{FN}_3\text{O}_3\text{S}^+$  456.2, found  $(\text{M})^+$  456.2. Melting point: 226  $^\circ\text{C}$ .

***N*-4-[[[2-[4-(aminosulfonyl) phenyl] ethyl] amino] carbonyl] benzyl-*N,N*-dimethyl-4-fluorobenzylammonium bromide (2)**

Following similar procedures as described above for the preparation of **1** by starting with **5** (155 mg, 0.3 mmol) and 4-(2-aminoethyl) benzenesulfonamide (80 mg, 0.4 mmol) in methanol (5 mL), 153 mg (93%) of **2** was obtained as white solid.  $^1\text{H NMR}$  (300 MHz, DMSO)  $\delta$  8.73 (t,  $J=5.5$  Hz, 1H), 7.94 (d,  $J=8.2$  Hz, 2H), 7.74 (d,  $J=8.2$  Hz, 2H), 7.71–7.60 (m, 4H), 7.53–7.33 (m, 4H), 7.30 (s, 2H), 4.63 (s, 4H), 3.55 (dd,  $J=12.8$ , 6.8 Hz, 2H), 2.94 (t,  $J=7.1$  Hz, 2H), 2.88 (s, 6H). MS (ESI) calculated for  $\text{C}_{25}\text{H}_{29}\text{FN}_3\text{O}_3\text{S}^+$  470.2, found  $(\text{M})^+$  470.2. Melting point: 215  $^\circ\text{C}$ .

***N*-4-[[[4-(aminosulfonyl) benzyl] amino] carbonyl] benzyl-*N,N*-dimethyl-4-fluorobenzylammonium bromide (3)**

Following similar procedures as described above for the preparation of **1** by starting with **5** (155 mg, 0.3 mmol) and 4-(aminomethyl) benzenesulfonamide (80 mg, 0.43 mmol) in methanol (5 mL), 160 mg (99%) of **3** was obtained as white solid.  $^1\text{H NMR}$  (300 MHz, DMSO)  $\delta$  9.29 (t,  $J=5.9$  Hz, 1H), 8.03 (d,  $J=8.2$  Hz, 2H), 7.77 (d,  $J=8.3$  Hz, 2H), 7.74–7.59 (m, 4H), 7.49 (d,  $J=8.3$  Hz, 2H), 7.37 (t,  $J=8.8$  Hz, 2H), 7.31 (s, 2H), 4.65 (s, 2H), 4.63 (s, 2H), 4.55 (d,  $J=5.8$  Hz, 2H), 2.88 (s, 6H). MS (ESI) calculated for  $\text{C}_{24}\text{H}_{27}\text{FN}_3\text{O}_3\text{S}^+$  456.2, found  $(\text{M})^+$  456.0. Melting point: 228  $^\circ\text{C}$ .

***N,N*-dimethyl-*N*-4-[(2,3,5,6-tetrafluorophenoxy) carbonyl] benzyl-4-(4,4,5,5-tetramethyl-1,3,2-dioxaborolan-2-yl)benzylammonium bromide (6)**

A mixture of **4** (2.15 g, 6.6 mmol) and 4-(bromomethyl) benzenboronic acid pinacol ester (1.95 g, 6.6 mmol) in acetonitrile (15 mL) was stirred at room temperature for 20 h. The resulting precipitate was filtered and washed with diethyl ether (10 mL  $\times$  3) to yield **6** as white solid (584 mg, 14%).  $^1\text{H NMR}$  (300 MHz, DMSO)  $\delta$  8.33 (d,  $J=8.4$  Hz, 2H), 8.15–7.98 (m, 1H), 7.90 (d,  $J=8.3$  Hz, 2H), 7.81 (d,  $J=8.0$  Hz, 2H), 7.62 (d,  $J=8.0$  Hz, 2H), 4.77 (s, 2H), 4.68 (s, 2H), 2.95 (s, 6H), 1.31 (s, 12H). MS (ESI) calculated for  $\text{C}_{29}\text{H}_{31}\text{BF}_4\text{NO}_4^+$  544.2, found  $(\text{M})^+$  544.3. Melting point: 179  $^\circ\text{C}$ .

***N,N*-dimethyl-*N*-4-[(2,3,5,6-tetrafluorophenoxy) carbonyl] benzyl-4-(4,4,5,5-tetramethyl-1,3,2-dioxaborolan-2-yl)benzylammonium trifluoromethanesulfonate (7)**

A solution of silver trifluoromethanesulfonate (232 mg, 0.9 mmol) in acetonitrile (3 mL) was added dropwise to a solution of **6** (562 mg, 0.9 mmol) in a mixture of acetonitrile (6 mL) and methanol (6 mL). The resulting solution was stirred for 4 h. The formed silver bromide precipitate was filtered through celite, and washed with methanol (5 mL  $\times$  2). The filtrate was concentrated under reduced pressure to yield **7** as light yellow solid (625 mg, 100%).  $^1\text{H NMR}$  (300 MHz,  $\text{CDCl}_3$ )  $\delta$  8.23 (d,  $J=8.2$  Hz, 2H), 7.87 (d,  $J=7.9$  Hz, 2H), 7.79 (d,  $J=8.3$  Hz, 2H), 7.50 (d,  $J=7.9$  Hz, 2H), 7.16–6.94 (m, 1H), 4.95 (s, 2H), 4.75 (s, 2H), 2.99 (s, 6H), 1.34 (s, 12H). MS (ESI) calculated for  $\text{C}_{29}\text{H}_{31}\text{BF}_4\text{NO}_4^+$  544.2, found  $(\text{M})^+$  544.3. MS (ESI) calculated for  $\text{CF}_3\text{O}_3\text{S}^-$  149.0, found  $(\text{M})^-$  149.0. Melting point: 108  $^\circ\text{C}$ .

***N*-4-[[[4-(aminosulfonyl) benzyl] amino] carbonyl] benzyl-*N,N*-dimethyl-4-(4,4,5,5-tetramethyl-1,3,2-dioxaborolan-2-yl)benzylammonium trifluoromethanesulfonate (8)**

A mixture of **7** (200 mg, 0.29 mmol) and 4-(2-aminoethyl) benzenesulfonamide (64 mg, 0.32 mmol) in methanol (6 mL) was stirred at room temperature for 20 h. The volatile solvent was removed under reduced pressure. Tetrahydrofuran (6 mL) was added to the residue, and the resulting mixture was sonicated for 5 min. The resulting precipitate was filtered, washed with tetrahydrofuran (1 mL  $\times$  2), and dried under reduced pressure to yield **8** as white solid (135 mg, 64%).  $^1\text{H NMR}$  (300 MHz, DMSO)  $\delta$  8.77–8.66 (m, 1H), 7.93 (d,  $J=6.9$  Hz, 2H), 7.80 (d,  $J=7.9$  Hz, 1H), 7.74 (d,  $J=8.2$  Hz, 2H), 7.71–7.63 (m, 2H), 7.63–7.51 (m, 3H), 7.43 (d,  $J=8.2$  Hz, 2H), 7.30 (s, 2H), 4.75–4.46 (m, 4H), 3.69–3.49 (m, 2H), 3.06–2.90 (m, 2H), 2.89 (d,  $J=12.6$  Hz, 6H), 1.31 (s, 6H). MS (ESI) calculated for  $\text{C}_{31}\text{H}_{41}\text{BN}_3\text{O}_5\text{S}^+$  578.3, found  $(\text{M})^+$  578.4. MS (ESI) calculated for  $\text{CF}_3\text{O}_3\text{S}^-$  149.0, found  $(\text{M})^-$  149.0. Melting point: 165  $^\circ\text{C}$ .

**Binding affinity measurement**

A stopped-flow method<sup>34</sup> has been used for assaying the CA catalyzed  $\text{CO}_2$  hydration activity with Phenol red as indicator, working at the absorbance maximum of 557 nm, following the initial rates of the CA-catalyzed  $\text{CO}_2$  hydration reaction for 10–100 s. For each inhibitor at least six traces of the initial 5–10% of the reaction have been used for determining the initial velocity. The uncatalyzed rates were determined in the same manner and subtracted from the total observed rates. Stock solutions of inhibitor (0.01 mM) were prepared in distilled-deionized water with 5% DMSO and dilutions up to 0.1 nM were done thereafter with the

assay buffer. The inhibition constant ( $K_i$ ) was obtained by considering the classical Michaelis–Menten equation, which has been fitted by non-linear least squares by using PRISM 3. All CA isozymes used in the experiments were purified human recombinant proteins obtained as reported earlier by our group<sup>35–45</sup>.

### Radiosynthesis of [<sup>18</sup>F]**2**

The <sup>18</sup>F-fluoride in H<sub>2</sub>[<sup>18</sup>O]O was passed through the QMA cartridge, and <sup>18</sup>F-fluoride was trapped and then eluted out with 0.3 mL aqueous solution of 5 mg tetrabutylammonium triflate into a 4-mL V-shaped reaction vial. Acetonitrile (1 mL) was added and the reaction vial was placed in a heating block and heated at 110 °C under vacuum for 6 min and subsequently under N<sub>2</sub> flow for another 6 min. A mixture of Cu(OTf)<sub>2</sub> (100 μL, 0.2 M), pyridine (500 μL, 1 M), and precursor (100 μL, 40 mM) solutions in *N,N*-dimethylformamide was added to the reaction vial. The reaction mixture was incubated at 110 °C for 20 min. The reaction was quenched with water (1 mL) and the resulted mixture was purified by HPLC using the semi-preparative column eluted with 24% CH<sub>3</sub>CN and 76% TEA-PB at a flow rate of 4.5 mL/min. The retention time of <sup>18</sup>F-labeled **2** was 17.6 min. The collected <sup>18</sup>F-labeled tracer was diluted with ammonium formate (50 mM, 50 mL), and trapped on a C<sub>18</sub> light Sep-Pak cartridge. The final product was eluted out with ethanol (0.4 mL), and formulated with saline (4 mL) for plasma stability, biodistribution, and PET/CT imaging studies. Quality control was performed by HPLC on the analytical column eluted with 25% CH<sub>3</sub>CN and 75% PBS at a flow rate of 2.0 mL/min. The retention time of <sup>18</sup>F-labeled **2** was 6.9 min. The specific activity of <sup>18</sup>F-labeled **2** was measured using the analytical HPLC system. It was calculated via dividing the injected radioactivity of <sup>18</sup>F-labeled tracer solution by the amount of the tracer in the injected solution. The amount of the tracer was calculated from the UV absorbance standard curve of non-radioactive **2**.

### LogD<sub>7.4</sub> measurement

The LogD<sub>7.4</sub> value of <sup>18</sup>F-labeled **2** was measured using the shake flask method as previously reported<sup>46</sup>. Briefly, an aliquot (2 μL) of <sup>18</sup>F-labeled **2** was added to a vial containing 3 mL of *n*-octanol and 3 mL of phosphate buffer (0.1 M, pH 7.4). The mixture was vortexed for 1 min and then centrifuged at 3000g for 10 min. Samples of the *n*-octanol (1 mL) and buffer (1 mL) layers were taken and counted in a well counter. LogD<sub>7.4</sub> was calculated using the following equation:  $\text{LogD}_{7.4} = \log_{10}[(\text{counts in } n\text{-octanol phase})/(\text{counts in buffer phase})]$ .

### Stability in mouse plasma

Stability in plasma was performed following published procedures<sup>47,48</sup>. Aliquots (100 μL) of <sup>18</sup>F-labeled **2** were incubated with 400 μL of balb/c mouse plasma (Innovative Research, Novi, MI) for upwards of 60 min at 37 °C. At the end of each incubation period, samples were quenched by addition of acetonitrile (0.5 mL), centrifuged to remove proteins, and finally passed through a 0.2 micron filter. The filtered samples were loaded onto the analytical radio-HPLC to check for metabolite formation, and analyses were conducted using Agilent ChemStation software.

### In vivo experiments

*In vivo* experiments were conducted in accordance with the guidelines established by the Canadian Council on Animal Care

and approved by the Animal Ethics Committee of the University of British Columbia. Male immunodeficient NOD.Cg-Prkdc<sup>scid</sup>Il2rg<sup>tm1Wjl</sup>/SzJ (NSG) mice were obtained from a breeding colony at the Animal Resource Centre of the BC Cancer Research Centre.

### Tumor implantation

Animal model was established following previously published procedures<sup>27</sup>. Under anesthesia with 2.5% isoflurane in 2.0 L/min of oxygen, mice were subcutaneously inoculated with 5 × 10<sup>6</sup> HT-29 cells (in 100 μL PBS and Matrigel at 1:1 ratio) under the right dorsal flank. Biodistribution studies and PET/CT imaging were performed when tumors reached 7–9 mm in diameter.

### PET imaging and biodistribution studies

For dynamic imaging study, tumor-bearing mice were sedated with 2% isoflurane inhalation and positioned prone onto the scanner bed. A 10 min baseline CT scan was obtained for localization and attenuation correction before radiotracer injection, using 60 kV X-rays at 500 mA, three sequential bed position with 33% overlap, and 220 degree continuous rotation. PET data were acquired in list mode acquisition, reconstructed using the 3d-OSEM-MAP algorithm with CT-based attenuation correction. The dynamic acquisition of 60 min was started at the time of intravenous injection with 6–8 MBq of the radiotracer. The list mode data were rebinned into time intervals (12 × 10, 6 × 30, 5 × 60, 6 × 300, and 2 × 600 s) to obtain tissue time-activity curves. The mice were kept warm by a heating pad during acquisition. For static imaging study, the mice were briefly sedated for intravenous injection of the radiotracer (6–8 MBq), and allowed to recover and roam freely in their cages for 45 min. At that point, the mice were sedated with 2% isoflurane inhalation, placed on the scanner, and an attenuation correction CT scan was obtained as described above. A single static emission scan was subsequently acquired for 10 min.

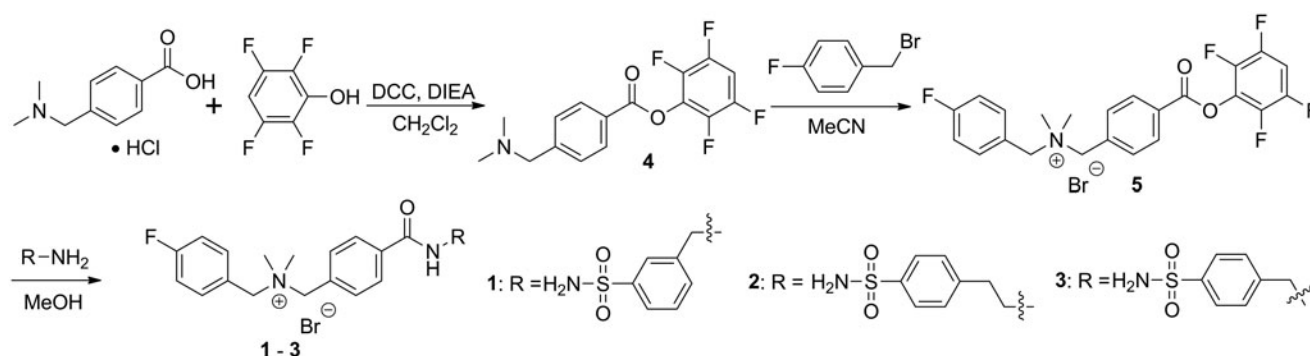
Biodistribution studies were performed to confirm the quantitative ROI uptake values observed from PET scans. At 1 h p.i., mice were euthanized. Blood was promptly withdrawn, and the organs/tissues of interest were harvested, rinsed with normal saline, blotted dry, and weighed. The radioactivity of the collected mouse tissues was counted and expressed as the percentage of the injected dose per gram of tissue (%ID/g).

## Results and discussion

As shown in Figure 2, the three cationic sulfonamides **1–3** were designed using 4-dimethylaminobenzoic acid as the linker to connect a 4-fluorobenzyl group and a benzenesulfonamide motif for CA-IX targeting. This design also generated the needed cationic quaternary ammonium group that would prevent free diffusion of **1–3** into cells and binding to intracellular CA isoforms including CA-I and CA-II. In addition, <sup>18</sup>F-labeled **1–3** could be prepared via copper-mediated aromatic radiofluorination reaction using an arylboronic pinacol ester precursor<sup>49,50</sup> as recently demonstrated by us for the preparation 4-[<sup>18</sup>F]fluorobenzyltriphenylphosphonium (<sup>18</sup>F-FBnTP), a myocardial perfusion PET tracer<sup>51</sup>.

The preparation of compounds **1–3** followed the procedures depicted in Scheme 1. The activated ester **4** was obtained in 99% yield by reacting 4-[(dimethylamino) methyl] benzoic acid with 2,3,5,6-tetrafluorophenol using *N,N'*-dicyclohexylcarbodiimide (DCC) as the coupling reagent. Reacting **4** with 4-fluorobenzyl bromide in acetonitrile afforded the quaternary ammonium bromide salt **5** as a precipitate which was isolated in 87% yield by





**Scheme 1.** Synthesis of cationic carbonic anhydrase IX inhibitors 1–3.

**Table 1.** Inhibition constants ( $K_i$ ) of cationic inhibitors 1–3 to carbonic anhydrases I, II, IV, and IX as determined by a stopped-flow  $\text{CO}_2$  hydration assay. Errors in the range of 5–10% of the reported value from three different assays.

Compound	Inhibition constant ( $K_i$ , $\mu\text{M}$ )			
	CA-I	CA-II	CA-IV	CA-IX
1	0.89	0.72	>50.0	0.44
2	0.52	0.07	9.54	0.22
3	0.78	0.48	3.63	0.96
Acetazolamide	0.25	0.01	0.08	0.03

filtration. The desired compounds **1–3** were obtained by coupling **5** in methanol with excess 3-(aminomethyl)benzenesulfonamide, 4-(2-aminoethyl)benzenesulfonamide, and 4-(aminomethyl)benzenesulfonamide, respectively. After evaporating methanol, the residue was triturated with tetrahydrofuran to obtain compounds **1–3** bromide salt in 93–99% yields.

After synthesis, the binding affinity of compounds **1–3** were evaluated for four physiologically relevant CAs: CA-I, -II, -IV, and -IX (Table 1). CA-I and CA-II are cytosolic isozymes that are found primarily in red blood cells, while CA-IV is a glycosyl-phosphatidylinositol anchored membrane isozyme found primarily in the eyes, lungs, and kidneys<sup>6</sup>. Compounds **1–3** exhibited different inhibitory profiles. The derivatives have inhibition constants ( $K_i$ ) in the ranges of 0.52–0.89, 0.07–0.72, 3.63–> 50, and 0.22–0.96  $\mu\text{M}$  for CA-I, -II, -IV, and -IX, respectively. Relative to acetazolamide ( $K_i(\text{CA-IX}) = 0.03 \mu\text{M}$ ), a pan CA inhibitor, the binding affinities of compounds **1–3** for CA-IX were substantially lower. With the best affinity towards CA-IX, compound **2** was selected for radiolabeling and *in vivo* experiments.

The preparation of the  $^{18}\text{F}$ -fluorination precursor **8** is shown in Scheme 2(A). Reacting the activated ester **4** with 4-bromomethylphenylboronic acid pinacol ester afforded the quaternary ammonium bromide salt **6** in 14% yield. The ammonium bromide salt **6** was treated with silver triflate and converted quantitatively to the ammonium triflate salt **7**. The desired precursor **8** was obtained in 64% by coupling **7** with 4-(2-aminoethyl)benzenesulfonamide.

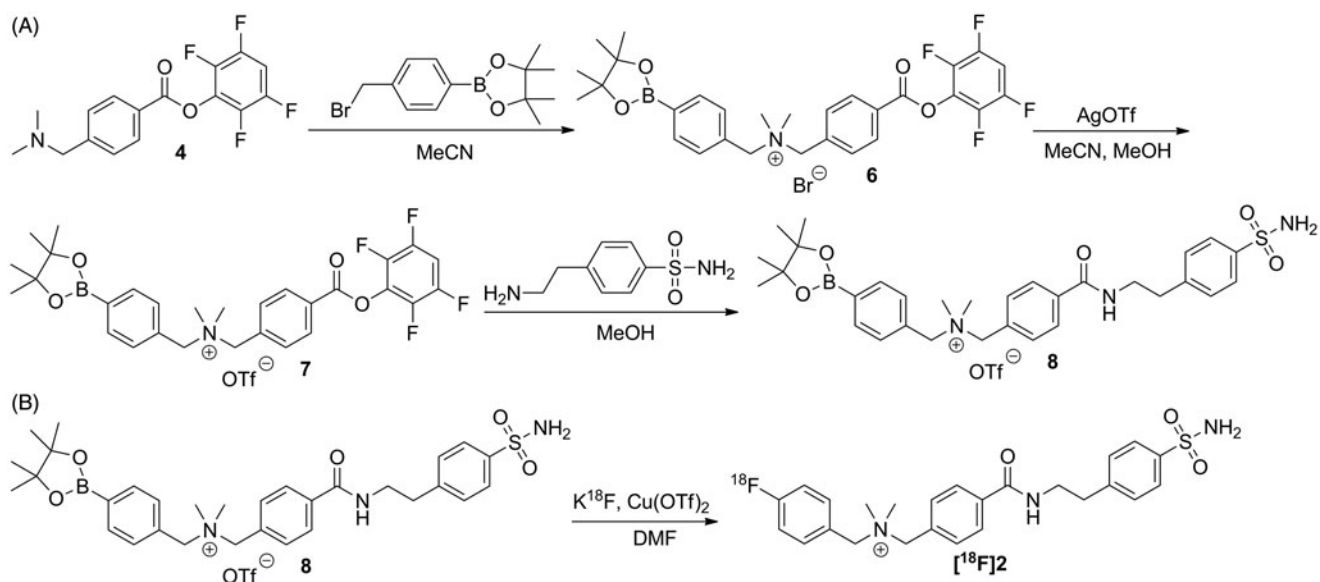
Synthesis of  $^{18}\text{F}$ -labeled **2** was performed by nucleophilic substitution of the precursor **8** with  $^{18}\text{F}$ -fluoride via copper-mediated aromatic radiofluorination reaction (Scheme 2(B))<sup>49–51</sup>. Purification and quality control of  $^{18}\text{F}$ -labeled **2** was performed by HPLC and  $^{18}\text{F}$ -labeled **2** was isolated in  $10 \pm 4\%$  ( $n = 3$ ) decay-corrected radiochemical yield with >98% radiochemical purity and  $85.1 \pm 70.3$  GBq/ $\mu\text{mol}$  specific activity. An *in vitro* stability study was conducted by incubating  $^{18}\text{F}$ -labeled **2** at  $37^\circ\text{C}$  in mouse plasma, and monitored by HPLC. As shown in Figure 3, no noticeable degradation of  $^{18}\text{F}$ -labeled **2** was observed after 60 min incubation,

suggesting high stability of  $^{18}\text{F}$ -labeled **2** in mouse plasma. Lipophilicity of  $^{18}\text{F}$ -labeled **2** was measured using traditional shake flask method<sup>46</sup>. The obtained  $\text{LogD}_{7.4}$  ( $D_{7.4}$ : distribution coefficient between *n*-octanol and pH 7.4 phosphate buffer) value was  $-0.79 \pm 0.02$ , indicating that the tracer was hydrophilic.

*In vivo* imaging experiments were conducted in immunodeficient NSG mice bearing HT-29 human colorectal cancer xenografts. Biodistribution data and representative PET/CT images acquired at 1 h post-injection are shown in Figures 4 and 5, respectively. Tracer uptake was predominantly observed in the excretory organs, liver ( $10.7 \pm 0.96\% \text{ID/g}$ ) and kidneys ( $13.7 \pm 3.96\% \text{ID/g}$ ). Moderate uptake was observed in HT-29 tumor xenografts ( $0.41 \pm 0.06\% \text{ID/g}$ ), which corresponded to tumor-to-muscle ratio of  $1.99 \pm 0.25$ . The lowest uptake was observed for the brain ( $0.02 \pm 0.00\% \text{ID/g}$ ), indicating that the tracer was unable to penetrate the blood–brain barrier. The tracer was stable against *in vivo* defluorination as uptake in bone was observed in negligible amount at  $0.13 \pm 0.02\% \text{ID/g}$ . PET images are consistent with biodistribution data, as the gastrointestinal tract and kidneys showed the highest accumulation of activity. HT-29 xenografts were visualized in PET images with moderate tumor-to-background contrast. Analyzing the time activity curve for  $^{18}\text{F}$ -labeled **2** (Figure 6), tracer was rapidly cleared through the kidneys and hepatobiliary tract. Despite moderate uptake, the uptake in tumor xenograft was higher compared to non-target tissues like bone, brain, and muscle, enabling its visualization in PET images.

The development of CA-IX targeting agents, particularly those derived from small molecule inhibitors has seen marked improvement in terms of tumor targeting and visualization. Initial efforts were hampered by the lack of target specificity, poor pharmacokinetics, and/or tracer instability<sup>24,25</sup>. Subsequently, our group and others have leveraged a radiometal-based approach to develop cell-impermeable tracers targeting CA-IX *in vivo*. Most recently, Pomper's group radiolabeled a dual motif CA-IX inhibitor consisting of a 4,4-bis(4-hydroxyphenyl)valeric acid and a succinyl acetazolamide group with  $^{111}\text{In}$  (via DOTA chelator) and  $^{64}\text{Cu}$  (via NOTA chelator) and achieved tumor uptakes values of 14.5–26.0%ID/g at 1 h p.i.<sup>29,30</sup>. Krall et al.<sup>31</sup> reported the synthesis and evaluation of a  $^{99\text{m}}\text{Tc}$ -labeled acetazolamide derivative with excellent tumor targeting (22%ID/g at 3 h p.i.) and image contrast. Notably, both research groups used the human renal-cell carcinoma SK-RC-52 model for *in vivo* evaluations. Renal cell carcinomas commonly overexpress CA-IX due to perturbations of the von Hippel-Lindau (*VHL*) gene, which in turn regulates HIF-1 $\alpha$ <sup>52–54</sup>. The expression of CA-IX in this model is not necessarily driven by hypoxia.

Beyond the use of radiometals, another major commonality shared by these successful tracers is the high affinity that they exhibit for CA-IX, typically with  $K_i$  values in the low



**Scheme 2.** (A) Synthesis of the radiolabeling precursor **8**. (B) Synthesis of  $^{18}\text{F}$ -labeled **2**.

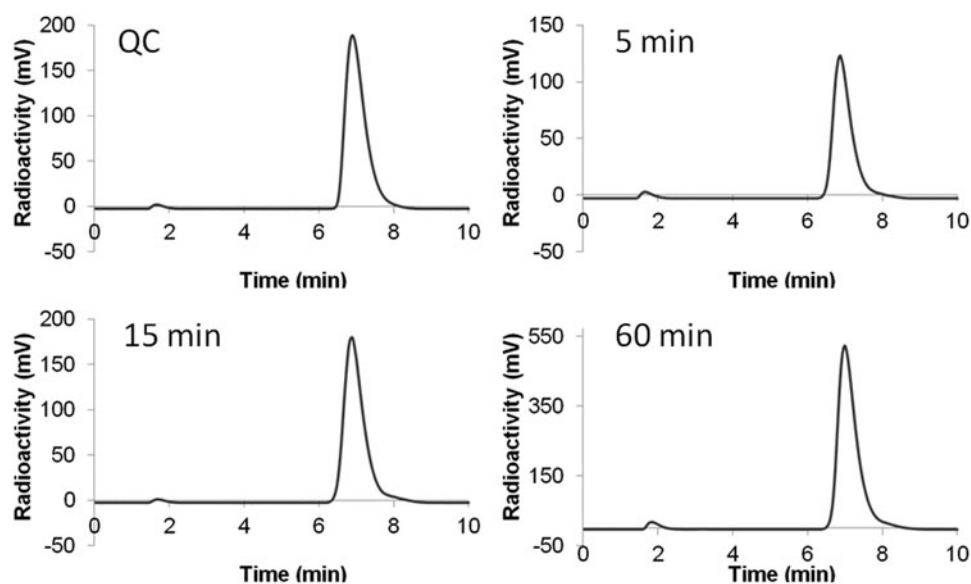


**Figure 3.** HPLC chromatograms of  $^{18}\text{F}$ -labeled **2** from (A) QC sample, or plasma sample after being incubated at  $37^\circ\text{C}$  for (B) 5 min, (C) 15 min, or (D) 60 min.

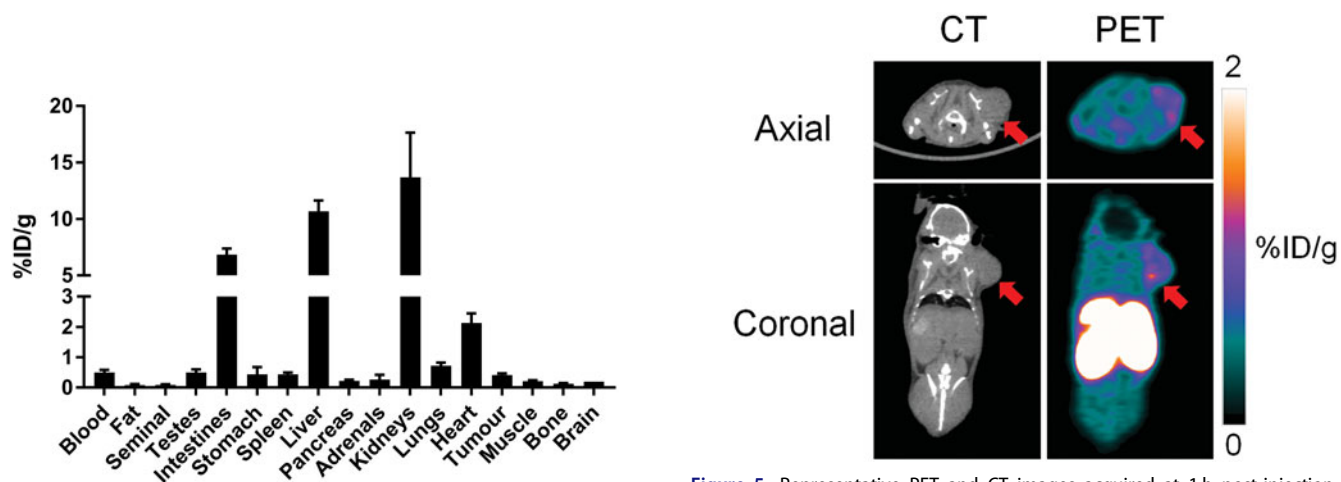


**Figure 4.** Biodistribution of  $^{18}\text{F}$ -labeled **2** at 1 h post-injection in HT-29 tumor-bearing mice. Values (%ID/g) are presented as mean  $\pm$  standard deviation ( $n = 5$ ).

**Figure 5.** Representative PET and CT images acquired at 1 h post-injection with  $^{18}\text{F}$ -labeled **2** in HT-29 colorectal cancer xenograft-bearing mice. Arrow indicates location of tumor.

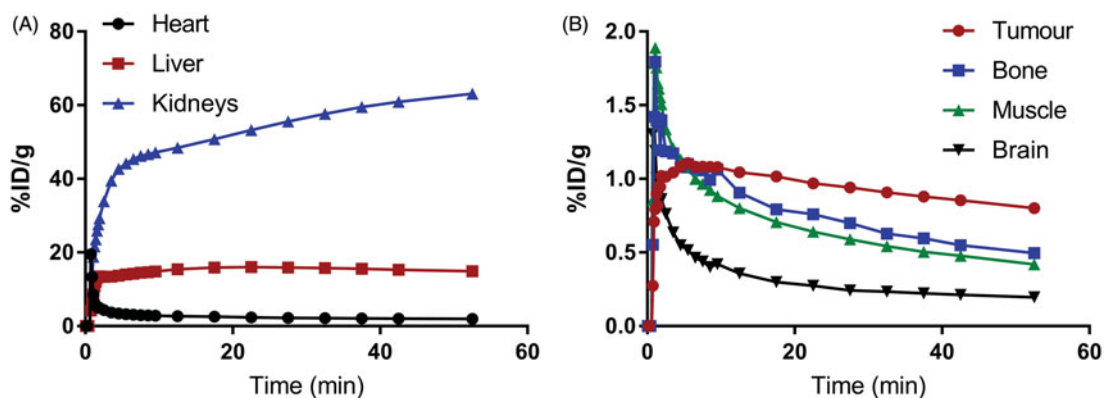


**Figure 6.** Time activity curves for  $^{18}\text{F}$ -labeled **2** using ROIs drawn around high activity organs (A) heart, liver, and kidneys, and low activity organs (B) tumor, bone, muscle, and muscle.

nanomolar range. On the contrary, compound **2** selected for radiolabeling and evaluated in this study had only moderate binding affinity to CA-IX ( $K_i = 0.22 \mu\text{M}$ ). A high binding affinity to the target of interest is one of many factors (stability, selectivity, target density, target accessibility, etc.) that determine efficient tumor targeting and accumulation<sup>55</sup>. Future studies leveraging the use of cationic sulfonamides to synthesize diagnostic agents targeting CA-IX require better understanding of the structure activity relationship to improve tracer affinity. The ability to visualize tumor notwithstanding the moderate uptake value suggests that cationic sulfonamides can potentially be used as pharmacophores for CA-IX imaging agents.

## Conclusion

We designed three cationic sulfonamide inhibitors **1–3** to potentially target CA-IX for PET applications. Imaging and biodistribution data for  $^{18}\text{F}$ -labeled **2** showed clear visualization of tumor xenografts despite moderate uptake and tumor-to-background contrast. This is encouraging considering the relatively modest binding affinity of **2** to CA-IX. Therefore, our data demonstrate the use of cationic motif may be useful for designing future CA-IX tracers assuming high affinity binders can be obtained.

## Acknowledgements

This work was supported by the Canadian Institutes of Health Research (FDN-148465) and the Leading Edge Endowment Fund. The authors would like to thank Wade English and Baljit Singh for their technical assistance.

## Disclosure statement

The authors report no conflicts of interest.

## Funding

This work was supported by the Canadian Institutes of Health Research (FDN-148465) and the Leading Edge Endowment Fund.

## References

- Vaupel P, Mayer A. Hypoxia in cancer: significance and impact on clinical outcome. *Cancer Metastasis Rev* 2007;26:225–39.
- Walsh JC, Lebedev A, Aten E, et al. The clinical importance of assessing tumor hypoxia: relationship of tumor hypoxia to prognosis and therapeutic opportunities. *Antioxid Redox Signal* 2014;21:1516–54.
- Wilson WR, Hay MP. Targeting hypoxia in cancer therapy. *Nature Rev Cancer* 2011;11:393–410.
- Brown JM. Tumor hypoxia in cancer therapy. *Meth Enzymol* 2007;435:297–321.
- Potter C, Harris AL. Hypoxia inducible carbonic anhydrase IX, marker of tumour hypoxia, survival pathway and therapy target. *Cell Cycle* 2004;3:164–7.
- Alterio V, Di Fiore A, D'Ambrosio K, et al. Multiple binding modes of inhibitors to carbonic anhydrases: how to design specific drugs targeting 15 different isoforms? *Chem Rev* 2012;112:4421–68.
- Robertson N, Potter C, Harris AL. Role of carbonic anhydrase IX in human tumor cell growth, survival, and invasion. *Cancer Res* 2004;64:6160–5.
- Hilvo M, Baranauskienė L, Salzano AM, et al. Biochemical characterization of CA IX, one of the most active carbonic anhydrase isozymes. *J Biol Chem* 2008;283:27799–809.
- Bartosova M, Parkkila S, Pohlodek K, et al. Expression of carbonic anhydrase IX in breast is associated with malignant tissues and is related to overexpression of c-erbB2. *J Pathol* 2002;197:314–21.
- Swietach P, Wigfield S, Cobden P, et al. Tumor-associated carbonic anhydrase 9 spatially coordinates intracellular pH in three-dimensional multicellular growths. *J Biol Chem* 2008;283:20473–83.
- Swietach P, Wigfield S, Supuran CT, et al. Cancer-associated, hypoxia-inducible carbonic anhydrase IX facilitates  $\text{CO}_2$  diffusion. *BJU Int* 2008;101:22–4.
- Lock FE, McDonald PC, Lou Y, et al. Targeting carbonic anhydrase IX depletes breast cancer stem cells within the hypoxic niche. *Oncogene* 2013;32:5210–19.
- Lou Y, McDonald PC, Oloumi A, et al. Targeting tumor hypoxia: suppression of breast tumor growth and metastasis by novel carbonic anhydrase IX inhibitors. *Cancer Res* 2011;71:3364–76.
- Pacchiano F, Carta F, McDonald PC, et al. Ureido-substituted benzenesulfonamides potently inhibit carbonic anhydrase IX and show antimetastatic activity in a model of breast cancer metastasis. *J Med Chem* 2011;54:1896–902.
- Toussin N, Maresca A, McDonald PC, et al. Glycosyl coumarin carbonic anhydrase IX and XII inhibitors strongly attenuate

- the growth of primary breast tumors. *J Med Chem* 2011; 54:8271–7.
16. Krall N, Pretto F, Decurtins W, et al. A small-molecule drug conjugate for the treatment of carbonic anhydrase IX expressing tumors. *Angew Chem Int Ed Engl* 2014;53: 4231–5.
  17. Cazzamalli S, Dal Corso A, Neri D. Linker stability influences the anti-tumor activity of acetazolamide-drug conjugates for the therapy of renal cell carcinoma. *J Control Rel* 2017; 246:39–45.
  18. Wichert M, Krall N. Targeting carbonic anhydrase IX with small organic ligands. *Curr Opin Chem Biol* 2015;26:48–54.
  19. Apte SD, Chin FT, Graves EE. Synthesis of a new PET radio-tracer targeting carbonic anhydrase IX. *J Labelled Comp Radiopharm* 2009;52:S408.
  20. Lu G, Hillier SM, Maresca KP, et al. Synthesis and SAR of novel Re-99mTc-labeled benzenesulfonamide carbonic anhydrase IX inhibitors for molecular imaging of tumor hypoxia. *J Med Chem* 2013;56:510–20.
  21. Akurathi V, Dubois L, Celen S, et al. Development and biological evaluation of (9)(9mTc-sulfonamide derivatives for in vivo visualization of CA IX as surrogate tumor hypoxia markers. *Eur J Med Chem* 2014;71:374–84.
  22. Akurathi V, Dubois L, Lieuwes NG, et al. Synthesis and biological evaluation of a 99mTc-labelled sulfonamide conjugate for in vivo visualization of carbonic anhydrase IX expression in tumor hypoxia. *Nuclear Med Biol* 2010;37: 557–64.
  23. Turkbey B, Lindenberg ML, Adler S, et al. PET/CT imaging of renal cell carcinoma with (18)F-VM4-037: a phase II pilot study. *Abdom Radiol (NY)* 2016;41:109–18.
  24. Pan J, Lau J, Mesak F, et al. Synthesis and evaluation of 18F-labeled carbonic anhydrase IX inhibitors for imaging with positron emission tomography. *J Enzyme Inhib Med Chem* 2014;29:249–55.
  25. Lau J, Pan J, Zhang Z, et al. Synthesis and evaluation of (18)F-labeled tertiary benzenesulfonamides for imaging carbonic anhydrase IX expression in tumours with positron emission tomography. *Bioorg Med Chem Lett* 2014; 24:3064–8.
  26. Lau J, Liu Z, Lin KS, et al. Trimeric radiofluorinated sulfonamide derivatives to achieve in vivo selectivity for carbonic anhydrase IX-targeted pet imaging. *J Nucl Med* 2015;56: 1434–40.
  27. Lau J, Zhang Z, Jenni S, et al. PET imaging of carbonic anhydrase IX expression of HT-29 tumor xenograft mice with (68)Ga-labeled benzenesulfonamides. *Molec Pharmaceut* 2016;13:1137–46.
  28. Sneddon D, Niemans R, Bauwens M, et al. Synthesis and in vivo biological evaluation of (68)Ga-labeled carbonic anhydrase IX targeting small molecules for positron emission tomography. *J Med Chem* 2016;59:6431–43.
  29. Yang X, Minn I, Rowe SP, et al. Imaging of carbonic anhydrase IX with an 111In-labeled dual-motif inhibitor. *Oncotarget* 2015;6:33733–42.
  30. Minn I, Koo SM, Lee HS, et al. [64Cu]XYIMSR-06: a dual-motif CAIX ligand for PET imaging of clear cell renal cell carcinoma. *Oncotarget* 2016;7:56471–9.
  31. Krall N, Pretto F, Mattarella M, et al. A technetium 99m-labeled ligand of carbonic anhydrase IX selectively targets renal cell carcinoma in vivo. *J Nucl Med* 2016;6:943–9.
  32. Casey JR, Morgan PE, Vullo D, et al. Carbonic anhydrase inhibitors. Design of selective, membrane-impermeant inhibitors targeting the human tumor-associated isozyme IX. *J Med Chem* 2004;47:2337–47.
  33. Basavaraj S, Betageri GV. Can formulation and drug delivery reduce attrition during drug discovery and development-review of feasibility, benefits and challenges. *Acta Pharmaceut Sinica B* 2014;4:3–17.
  34. Khalifah RG. The carbon dioxide hydration activity of carbonic anhydrase. I. Stop-flow kinetic studies on the native human isoenzymes B and C. *J Biol Chem* 1971;246:2561–73.
  35. Yamali C, Gul HI, Sakagami H, Supuran CT. Synthesis and bioactivities of halogen bearing phenolic chalcones and their corresponding bis Mannich bases. *J Enzyme Inhib Med Chem* 2016;31:125–31.
  36. Mollica A, Locatelli M, Macedonio G, et al. Microwave-assisted extraction, HPLC analysis, and inhibitory effects on carbonic anhydrase I, II, VA, and VII isoforms of 14 blueberry Italian cultivars. *J Enzyme Inhib Med Chem* 2016;31:1–16.
  37. Margheri F, Ceruso M, Carta F, et al. Overexpression of the transmembrane carbonic anhydrase isoforms IX and XII in the inflamed synovium. *J Enzyme Inhib Med Chem* 2016; 31:60–3.
  38. Mishra CB, Kumari S, Angeli A, et al. Design, synthesis and biological evaluation of N-(5-methyl-isoxazol-3-yl)-1,3,4-thiadiazol-2-yl)-4-(3-substitutedphenylureido) benzenesulfonamides as human carbonic anhydrase isoenzymes I, II, VII and XII inhibitors. *J Enzyme Inhib Med Chem* 2016;31:174–9.
  39. Diaz JR, Fernandez Baldo M, Echeverria G, et al. A substituted sulfonamide and its Co (II), Cu (II), and Zn (II) complexes as potential antifungal agents. *J Enzyme Inhib Med Chem* 2016;31:51–62.
  40. Supuran CT, Kalinin S, Tanc M, et al. Isoform-selective inhibitory profile of 2-imidazoline-substituted benzene sulfonamides against a panel of human carbonic anhydrases. *J Enzyme Inhib Med Chem* 2016;31:197–202.
  41. Federici C, Lugini L, Marino ML, et al. Lansoprazole and carbonic anhydrase IX inhibitors synergize against human melanoma cells. *J Enzyme Inhib Med Chem* 2016;31:119–25.
  42. Chohan ZH, Scozzafava A, Supuran CT. Unsymmetrical 1,1'-disubstituted ferrocenes: synthesis of Co(ii), Cu(ii), Ni(ii) and Zn(ii) chelates of ferrocenyl -1-thiadiazolo-1'-tetrazole, -1-thiadiazolo-1'-triazole and -1-tetrazolo-1'-triazole with antimicrobial properties. *J Enzyme Inhib Med Chem* 2002; 17:261–6.
  43. Del Prete S, Vullo D, Fisher GM, et al. Discovery of a new family of carbonic anhydrases in the malaria pathogen *Plasmodium falciparum* – the eta-carbonic anhydrases. *Bioorg Med Chem Lett* 2014;24:4389–96.
  44. Supuran CT, Scozzafava A, Mastrolorenzo A. Bacterial proteases: current therapeutic use and future prospects for the development of new antibiotics. *Expert Opin Ther Pat* 2001;11:221–59.
  45. Supuran CT, Barboiu M, Luca C, et al. Carbonic anhydrase activators. 14. Syntheses of mono and bis pyridinium salt derivatives of 2-amino-5-(2-aminoethyl)- and 2-amino-5-(3-aminopropyl)-1,3,4-thiadiazole and their interaction with isozyme II. *Eur J Med Chem* 1996;31:597–606.
  46. Lin KS, Pan J, Amouroux G, et al. In vivo radioimaging of bradykinin receptor b1, a widely overexpressed molecule in human cancer. *Cancer Res* 2015;75:387–93.
  47. Amouroux G, Pan J, Jenni S, et al. Imaging bradykinin B1 receptor with 68Ga-labeled [des-Arg10]Kallidin derivatives: effect of the linker on biodistribution and tumor uptake. *Molec Pharmaceut* 2015;12:2879–88.



48. Liu Z, Amouroux G, Zhang Z, et al. (18)F-trifluoroborate derivatives of [des-arg(10)]kallidin for imaging bradykinin b1 receptor expression with positron emission tomography. *Mol Pharmaceut* 2015;12:974–82.
49. Tredwell M, Preshlock SM, Taylor NJ, et al. A general copper-mediated nucleophilic 18F fluorination of arenes. *Angew Chem Int Ed Engl* 2014;53:7751–5.
50. Mossine AV, Brooks AF, Makaravage KJ, et al. Synthesis of [18F]Arenes via the copper-mediated [18F]fluorination of boronic acids. *Organic Lett* 2015;17:5780–3.
51. Zhang Z, Zhang C, Lau J, et al. One-step synthesis of 4-[(18)F]fluorobenzyltriphenylphosphonium cation for imaging with positron emission tomography. *J Labelled Comp Radiopharm* 2016;59:467–71.
52. Stillebroer AB, Mulders PF, Boerman OC, et al. Carbonic anhydrase IX in renal cell carcinoma: implications for prognosis, diagnosis, and therapy. *Eur Urol* 2010;58:75–83.
53. Chrastina A, Zavada J, Parkkila S, et al. Biodistribution and pharmacokinetics of 125I-labeled monoclonal antibody M75 specific for carbonic anhydrase IX, an intrinsic marker of hypoxia, in nude mice xenografted with human colorectal carcinoma. *Int J Cancer* 2003;105:873–81.
54. Ivanov SV, Kuzmin I, Wei MH, et al. Down-regulation of transmembrane carbonic anhydrases in renal cell carcinoma cell lines by wild-type von Hippel-Lindau transgenes. *Proc Natl Acad Sci USA* 1998;95:12596–601.
55. Srinivasarao M, Galliford CV, Low PS. Principles in the design of ligand-targeted cancer therapeutics and imaging agents. *Nature Rev Drug Discov* 2015;14:203–19.